Two-channel direct-detection Doppler lidar employing a charge-coupled device as a detector

Todd D. Irgang, Paul B. Hays, and Wilbert R. Skinner

A direct-detection Doppler lidar system is demonstrated that uses a CCD as a detector for the first time to our knowledge. The ability to use this linear device with the circular output from a Fabry–Perot etalon comes from use of a circle-to-line converter [Appl. Opt. **29,** 1482 (1990)]. In addition to the gains in quantum efficiency obtained through use of this detector, the lidar system described in this paper also has the capability to measure winds from aerosol and molecular backscatter simultaneously in two separate channels by directing the light reflected from one channel into the other. Early measurements with this system are presented; it is shown that, although accurate aerosol wind measurements are easily obtained, molecular measurements require a carefully calibrated inverse model and special hardware to derive accurate wind measurements with this channel.

OCIS codes: 280.3640, 050.2230, 280.1100, 010.3640, 040.1520.

1. Introduction

Measurements of the state parameters of the atmosphere (temperature, humidity, and wind velocities) at altitudes spanning the entire troposphere are essential to provide increased accuracy of weather predictions. Most of these measurements are currently made with radiosondes that are launched twice daily at many points around the globe. Each balloon acquires a measurement of the state parameters at a series of discrete altitudes through the atmosphere. The sondes are typically launched over land, although some are deployed from shipborne or airborne platforms. In any case, these data are exceptionally scant over oceans and other sparsely populated areas.

Satellite measurements have filled in many of the data voids left by balloon measurements. Uniform coverage of temperature and humidity from the ground to ~20 km is provided twice daily by polar-orbiting meteorological satellites[1]; however, there is currently no altitude resolution of winds at multiple layers of the lower atmosphere. Nonetheless, range-resolved wind velocities are perhaps the key parameter necessary for the improvement of long-range weather forecasting.[2] A technique that promises to deliver such velocity measurements is the lidar technique. Doppler lidar technology is well established, with wind measurements from ground-based lidars having first been made in the late 1960s.[3] An extensive series of papers has discussed the possibility of making these measurements from an orbital platform.[4–7] Both the direct-detection lidar (DDL)[8–10] and the heterodyne-detection lidar[11,12] methods have been proposed in these studies. However, technological limitations require that heterodyne-detection lidars operate in the infrared, which limits their use to wind measurements from aerosol backscatter.[13] DDLs require larger collection optics and higher laser powers than their heterodyne-detection lidar counterparts,[14] but DDLs have the capability to resolve both molecular and aerosol backscatter. This allows measurements to be made, for example, in the aerosol-devoid upper troposphere, where atmospheric weather patterns are largely driven.

DDLs use a spectroscopic element (usually a Fabry–Perot interferometer) to resolve the wavelength of the Doppler-shifted light. This spectroscopic element must be either scanned in wavelength,[8,9,15] or have an extremely well-known spectral response,[16] as winds of a few meters per

When this research was performed, T. D. Irgang (tirgang@visteon.com), P. B. Hays, and W. R. Skinner were with the Department of Atmospheric, Oceanic, and Space Sciences, Space Physics Research Laboratory, University of Michigan, 2455 Hayward, Ann Arbor, Michigan 48109-2143. T. D. Irgang is now with Visteon Technology Center—Glendale, 24300 Glendale Avenue, Redford, Michigan 48239. P. B. Hays is with the Michigan Aerospace Corporation, 1777 Highland Drive, Suite B, Ann Arbor, Michigan 48108.

Received 25 June 2001; revised manuscript received 17 October 2001.

0003-6935/02/061145-11$15.00/0

second cause Doppler shifts of the order of only a few femtometers in wavelength. There are two limitations that DDLs have experienced to this point. First, although a DDL can have the capability to resolve both aerosol and molecular backscatter, the spectral widths of these signals are orders of magnitude different, and an interferometer must be optimized for either one or the other. This has limited DDL systems to date to the measurement of only one component of backscatter or the other. Second, interferometers reflect out most of the light that enters them. The transmission of a Fabry–Perot optimized for aerosol backscatter is of the order of 10%, with the other 90% typically unutilized. Because wind measurement accuracy is dependent on the amount of signal collected, this inefficiency of the Fabry–Perot can limit the overall signal-to-noise ratio, as well as the maximum altitude range that can be achieved.

In an effort to increase overall system efficiency, the University of Michigan (U of M) has developed a lidar system that uses a 30-cm air-gapped Fabry–Perot to make high-spectral-resolution measurements from aerosol-backscattered returns. Then, with a technique similar to that described by Skinner and Hays,[17] the reflected light from this etalon is captured and reflected into another etalon with a much wider passband to enable Doppler measurements from molecular-backscattered light. In addition, the reflected light from this etalon is captured to provide photometric information to further supplement the wind measurements. In this way, nearly all the light that enters the detection system is utilized.

A further significant gain in collection efficiency can be realized by use of a CCD as the detector. DDL measurements to date have been made only with photomultiplier-type devices, which have much lower quantum efficiencies than CCDs (which range from 40–90%). However, CCDs are not readily incorporated into Doppler lidar systems because the detection elements are arranged in a rectangular pattern, and the light output from a Fabry–Perot forms a circular pattern. This problem has been solved through use of a reflective 90° cone segment[18] to convert the circular output from the Fabry–Perot into a linear arrangement of spots on the CCD detector (Fig. 1). Altitude resolution is then obtained when the light distribution on the detector is shifted along an axis perpendicular to the cone axis.

Our primary objectives in this paper are twofold. The first objective is to demonstrate the successful implementation of a CCD detector in a DDL by use of the circle-to-line interferometer optical system (CLIO) cone. The second objective is to show that the reflected light from an aerosol-optimized etalon can be captured and used in an etalon optimized for molecular backscatter. In Section 2 a complete description of the instrument used to demonstrate these technologies is presented. In Section 3, the technique used to collect and process the data from the CCD is described in detail, with the first measurements from the system presented in Section 4.

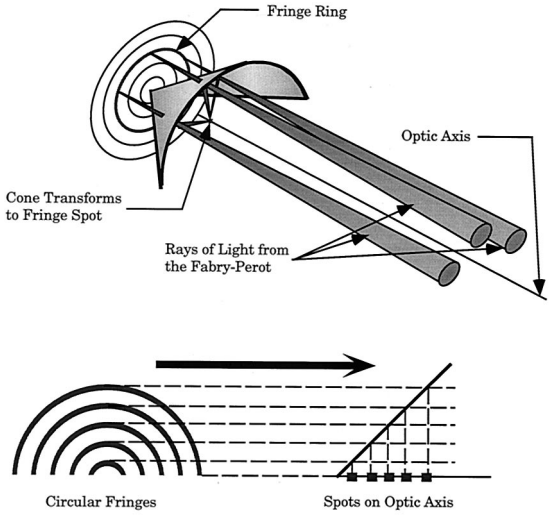

Fig. 1. CLIO transform. With the apex on the optic axis, the cone segment maps light along a radial segment into a single spot along the axis of the cone.

Some limitations of the instrument as implemented are also described in Section 4, along with suggestions to overcome these limitations.

2. Instrument Description

The U of M Doppler lidar system described in this paper is the second lidar instrument developed at U of M. The first instrument has been described extensively elsewhere.[8,19,20] The new lidar system was developed to improve the overall detection efficiency by approximately 2 orders of magnitude. A brief description of the present system is given here, and a more complete description can be found in Irgang.[21]

Figure 2 shows the instrument layout. The laser is an injection-seeded[22] Nd:YAG laser, frequency tripled to 355 nm. This wavelength was chosen over 1064 and 532 nm because the possibility of eye damage is greatly reduced. Relevant laser properties are given in Table 1. A series of dichroic mirrors directs the laser light through the center of a 44.5-cm-diameter Cassegrain telescope. This telescope is mounted on a large aluminum plate that reduces the amount of stray light entering the cargo trailer in which the receiving optics are located. The plate is mounted on a circular bearing that allows the telescope assembly to rotate to face any azimuthal angle. A fiber-glass dome encompasses the telescope and is slaved to rotate with the bearing. At the output of the telescope a 2× beam expander is used to match the etendue of the outgoing beam to that of the receiving optics. Along the entire outgoing optical path, the beam is encased by baffle tubes to prevent scattered light from entering the detection system.

Backscattered light is collected by the telescope and imaged through a −100-mm focal-length lens onto a 2-mm-long, 1-mm-diameter fiber optic. The lens extends the telescope focal length from 200 to 400 cm to match the etendue of the telescope to the remainder of the receiving optics. A 15.2-cm-

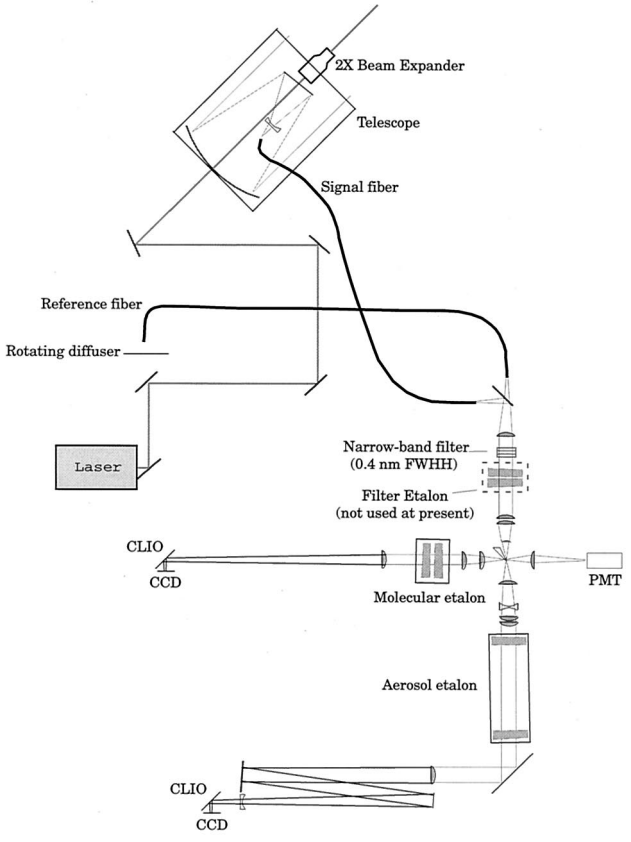

Fig. 2. Complete optical system diagram for the new U of M Doppler lidar instrument. FWHH, full width at half-height.

diameter secondary was used, and the focus of the telescope was placed behind the secondary mirror at an intermediate position. Outgoing light was directed through the center of the telescope for ease of alignment. The 2.0-cm-diameter hole through each of the mirrors was made large enough to permit a baffle tube to pass through the mirror and enclose the outgoing beam to prevent scattered light from entering the telescope. A kinematic aluminum structure supports all the elements contained in the telescope.

The fiber optic from the telescope transmits the light to a beam-splitter assembly, where the reference light and signal light are combined to be oriented along the same optical axis. The reference light comes from the back of the second output mirror and is focused onto a shorter 1-m-length fiber, as illustrated in Fig. 2. A rotating diffuser is used to efficiently scramble the light entering this fiber optic. After passing through the beam splitter, the light is expanded and collimated to illuminate the Fabry–Perot etalons. Data on each of the etalons are presented in Table 2. Each etalon is housed in a sealed canister filled with heated (30 °C) dry nitrogen and temperature regulated to within 0.1 °C of the setpoint.

Table 1. Laser Parameters

Type	Continuum PowerLite 8030 Injection-Seeded Nd:YAG
Wavelength	355 nm (frequency tripled from 1064 nm)
Linewidth	0.0038 cm^{-1} (110 MHz; 4.8×10^{-5} nm)
Pulse length	7 ns (2 m)
Repetition rate	30 Hz
Energy per pulse	150 mJ
Output power	4.5 W
Beam divergence	0.5 mrad (full angle)

Table 2. Lidar Etalon Data

Etalon Parameter	Filter Etalon	Aerosol Etalon	Molecular Etalon
Diameter (mm)	50.8	65	65
Plate spacing (mm)	1	300	8
Reflectivity at 355 nm	0.89	0.77	0.575
Reflectivity finesse	26.9	12.0	5.61
Free spectral range (cm^{-1})	5.00	0.0167	0.625
Flatness (coating)	$\lambda/100$	$\lambda/100$	$\lambda/100$

The etalons are mounted on a vertical optical bench, with light from the receiving optics passing first through the filter etalon. Preceding this etalon is a 0.43-nm full width at half-height narrow-band filter with a maximum transmission of 42% and a wideband filter (Schott UG-5). These, in combination with the 355-nm reflecting dichroic mirrors in the receiving optics chain, ensure that nearly all the solar background is removed prior to this etalon. The filter etalon has a 1-mm plate spacing and acts as a narrow-band filter in reducing light from the sidebands of the other etalons (multiple etalon filtering has been described elsewhere).[19,23,24] The net attenuation of sideband transmission is ~99%.

After passing through the filter etalon, the light continues on through one of three paths. It is either transmitted through the aerosol etalon, transmitted through the molecular etalon by reflection from the aerosol etalon, or reflected from the molecular etalon (Fig. 3). This particular arrangement uses nearly all the light that passes through the filter etalon, minus a small amount that is scattered or absorbed. Because most of the light entering an etalon is reflected out,[25] only ~13% of the light is transmitted through the aerosol system. The remaining 87% is collected by the pickoff mirror and passes into the molecular etalon. Here approximately 43.5% of the remaining light is transmitted, and the reflected energy from this etalon then goes into the reflected molecular system. Because a third CCD detector was not available, the remaining light reflected from the molecular etalon was imaged onto a photomultiplier tube (PMT) detector to provide additional measurement of the photometric return. A slight defocusing of the molecular collimator was performed to remove modulation that was due to the aerosol channel. The defocusing had little effect on the molecular image because of the factor of ~36 difference between the focal lengths of the imaging optics in two channels.

Once the light passes through the Fabry–Perot sys-

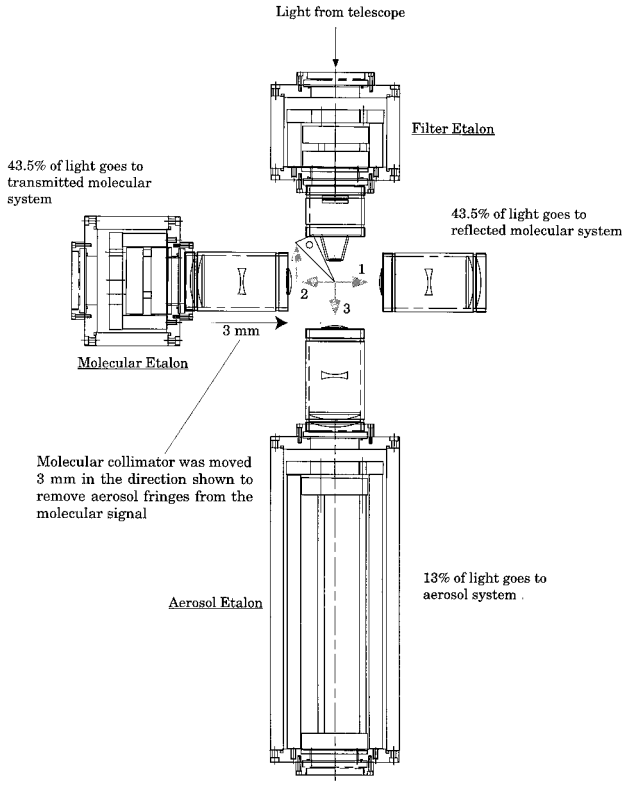

Fig. 3. Etalon beam-divider section. The base of each arrow represents the apex of the 90° wedge segment. Light initially passes downward through the aerosol etalon with orientation 1. The reflected light from the aerosol etalon has orientation 2 and is captured by the pickoff mirror and passes through the molecular etalon oriented as in the upperward-pointing arrow next to arrow 2. Light reflected from the molecular etalon has orientation 3 and is also captured and used in this system.

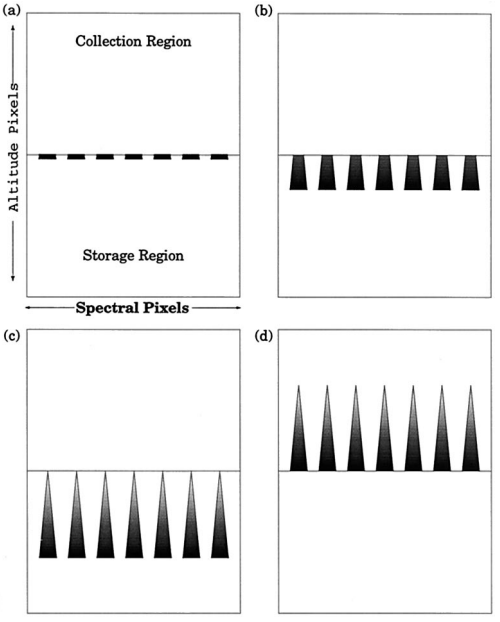

Fig. 4. CCD collection timing: (a) the charge has just begun to accumulate at the center of the array, (b) the return signal has been obtained over half of the altitude range, (c) the last altitude has been collected for the first shot of the laser, and (d) is then reverse shifted to the starting position for the collection of the second laser pulse.

tem, it is imaged onto two separate CCD cameras. Each CCD is 576 pixels long by 384 pixels wide, with a pixel size of 22 μm on a side. Altitude resolution in this system is obtained when the charge on the CCD is shifted in one direction until the return light has sufficiently diminished to background levels and then is reverse shifted back to the start position as indicated in Fig. 4. This process, first used by Povey *et al.*[26] in a differential absorption lidar and differential optical absorption system application, allows several consecutive laser pulses to be collected on the chip. Building up the signal on the chip lessens the effect of read noise, thereby improving the signal-to-noise ratio. Because charge can be shifted around on the CCD much faster than it can be read off and digitized, data collection efficiency is also increased the longer the charge is integrated on the chip. Integration for too long a period would result in pixels being filled to full well capacity, resulting in the loss of spectral information. It was found that a duty cycle of 1 s was reasonable, with on-chip integration performed during the first 27 laser pulses and readout performed during the remaining three. Each CCD has an electronic shutter immediately in front of the entrance aperture that is closed during readout periods.

The CCDs are thermoelectrically cooled to approximately −50 °C, with the excess heat generated by the thermoelectrics removed by refrigerated water. Dark charge accumulates slowly with the CCDs cooled to this temperature [5 e^- (pixel/s)]. The effect of read noise (12 e^-/digitization) is reduced when the 384 pixels are binned in each spectral row down to 96, which also reduces the readout time by a factor of 4. The binning pattern used is nonuniform and was chosen to be approximately linear in wavelength. Perfect linearity is not possible, but this effect is easily compensated for in the data analysis.[21] The charge-transfer efficiency of the CCDs was determined to be dependent on the number of electrons (counts) contained in each pixel and the rate at which the charge was transferred. The measured charge-transfer efficiency was better than 0.999999 for the typical count levels expected on the CCD.

3. Data Collection

A complete timing diagram for the system is shown in Fig. 5. An industry-standard architecture board for a personal computer was produced in house to generate the timing pulses to the laser and the CCD cameras. The shutter is preopened prior to the flash-lamp firing to ensure that all of the first laser pulse is captured. Between the flash-lamp firing and the *Q*-switching, a pulse is sent to the CCD to initiate its shifting process. This is done to separate the dwell region of the CCD from the portion of the CCD where the return signal is collected and stored. The CCD is shifted a total of 100 pixels, where it dwells for another period (~16.2 ms) before a pulse is

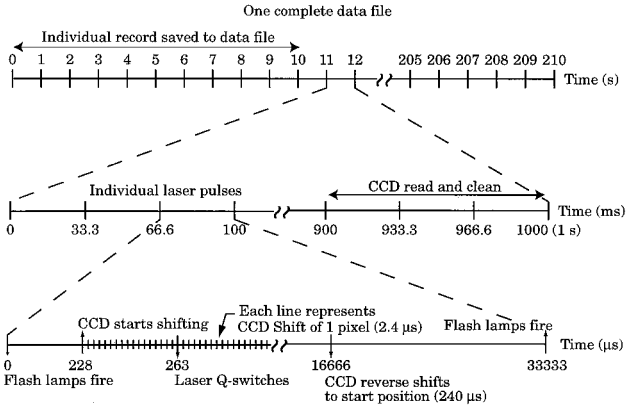

Fig. 5. Timing diagram for data collection on three different time scales.

received that signals the CCD to shift back to the start position. After this cycle is repeated 27 times, the shutter is closed and the charge that has accumulated on the CCD is read out and digitized. Readout takes significantly longer than the shifting process, and a full two shots of the laser takes place during this time. The chip is cleaned during the last shot of each second, at which point the shutter is again preopened and the cycle is repeated.

The 1-s data read from the chip are stored in memory and added to the nine subsequent readouts before the data are stored to disk in a data file. The data from the CCDs have an attached header that contains information relating to the status of the system, such as the temperatures of the laser, room, and etalons, the pressure of the etalon chambers, the azimuth angle of the beam and telescope, and the date and time. Only twenty-one 10-s integrations (3.5 min of data) with status headers are stored in each data file to maintain the files to a reasonable size (~1 Mbytes). Two separate computers are connected to two individual CCD controllers that are used to issue commands to each CCD chip. These controllers were fabricated by Princeton Instruments (now Roper Scientific) and were designed to allow high-speed and reverse-direction shifting of the charge on a standard image-zone CCD camera. The CCD data along with the status data from the control computer are all transferred to a fourth computer for storage and display. The display allows the user to monitor the data to ensure that the lidar is operating properly. A fifth computer collects data from a PMT detector mounted in the reflected molecular channel. This allows monitoring of the photometric return, which is extremely useful to determine whether the laser is well aligned with the axis of the telescope. The PMT data are also useful to determine whether a cloud is in the lidar field of view, which would render data near the cloud altitude useless.

For simplicity, the first measurements with this system were restricted to nighttime only, one-component measurements of the winds. Data files were collected in five different modes: background, reference-only, signal-only, normalization, and standard data. The background, reference-only, and normalization files were collected every two hours during the nights that data collection was performed. Background files were collected with the instrument in its standard operating mode, but with the laser shuttered to prevent laser light from entering the atmosphere. This provided a measurement of the background light from the sky, along with the combined effects of dark counts, bias, and read noise of the CCD chip. The reference-only mode was used to provide a measurement of the spectral response of the CCD to the reference spectrum. The signal fiber was blocked for this measurement, and the only light reaching the detector was due to laser light piped directly through the reference fiber optic. For the signal-only mode, the reference signal was blocked, and only return light from the sky was collected. The combination of the signal-only and return-only data was used to determine the relative contribution of each to the signal in regions where these two spectra overlapped (the lowest kilometer of data). Normalization data were collected with the laser unseeded to provide a spectral return that was essentially flat over the bandpass of the etalons. This was used to determine the intensity distribution on the detector, which was nonuniform. Most of this nonuniformity was due to the uneven binning of the CCD—e.g., one bin might have three pixels worth of data, whereas each adjacent bin has two. Use of a single fiber optic to transfer light to the detection system also contributed to this nonuniform response because perfect scrambling cannot be achieved with a single fiber strand. The normalization data were thus used to correct the standard data to provide a spectral response that was approximately uniform over the detector.

The data were processed in approximately two-hour blocks because new background and normalization files were collected approximately that often. The background image was read in first and subsequently subtracted from the normalization and standard data files. Each row of the normalization data was then divided by the maximum number of counts in that row, so that the channel with the most counts had a value of one. We then corrected the standard data files for intensity nonuniformities by dividing by this normalization data. The net result of these operations is shown in Fig. 6, where an uncorrected spectrum is shown, along with the same spectrum with background subtraction and normalization performed.

Wind measurements were effected by use of a discrete Fourier transform (DFT) and a comparison of the phase shift of the return spectrum with that of the reference spectrum. The velocity shift for a given range bin was found by the equation

$$\Delta u = \frac{\Delta u_{\mathrm{fsr}}(\Theta_r - \Theta_0)}{2\pi}, \tag{1}$$

where Δu_{fsr} is the velocity free spectral range (88.75 and 3328 m/s for the aerosol and molecular channels,

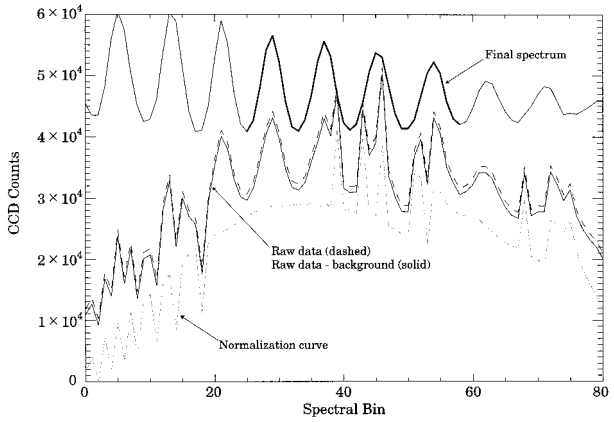

Fig. 6. Spectrum from 1-km altitude on 7 October 1999 at 1:09 a.m. EDT. The raw data were background subtracted and then divided by the normalization curve (offset −11000 counts from true position for clarity) to produce the final spectrum as shown. The bold segment of the final spectrum curve represents the portion of the curve from which wind measurements are derived.

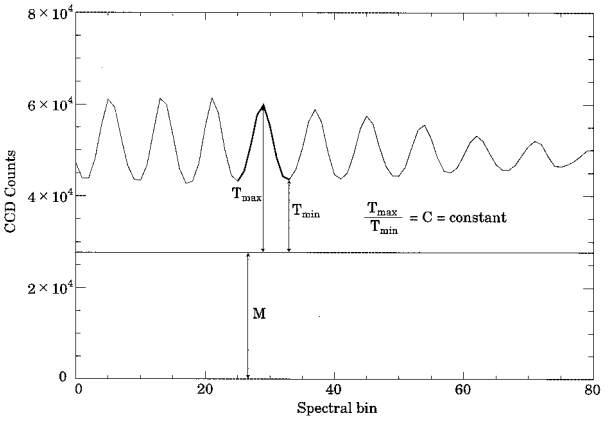

Fig. 7. Spectrum from 11:28 p.m. EDT on 6 October 1999. The spectrum was split into molecular and aerosol parts by Eq. (2).

respectively) and Θ_r, Θ_0 are the phases determined by the DFT for the range signal and reference signal, respectively.

It has been shown previously[18] that the width of the line on the detector increases with distance from the apex of the CLIO cone because of conservation of etendue. The effect of this phenomenon is that data from lower spectral bins overlap more altitudes than do data from higher spectral bins. However, the higher spectral bins collect less light because the image of the fiber optic projected onto the detector is circular rather than wedge shaped as would be the ideal situation.[17] This results in the signal amplitude being much smaller in these spectral bins. Thus, because of these problems and the simple inversion technique that was employed, only a portion of the fringes collected on the detector was used for the actual wind measurement. The bold segment of the final spectrum curve in Fig. 6 represents an actual portion of a spectrum on which the DFT analysis was performed. The analysis software searched for minima in the reference spectrum and used the segment between the fourth and the eighth minima to perform the fit. Zero (ground) altitude was chosen as the center of the reference line. Because the reference signal was approximately five pixels wide at this point, the reference signal was determined by an average of the center spectrum with the spectra from the two rows above and the two rows below the zero altitude line. The average was weighted according to the strength of the reference signal in each row as determined from the reference-only-mode data. A similar averaging was performed for each row of the standard data signal. We determined weighting in this case by sending direct laser light into the signal fiber prior to installation of the fiber into the telescope. The DFT was then performed on the reference spectrum to determine its phase, and the same spectral bins of each subsequent row were used to determine the phase of the return signal. Velocity was then determined by Eq. (1).

Determination of the aerosol/molecular (A/M) ratio has proven useful in prior studies[19,20] and is determined easily from the aerosol etalon signal. Figure 7 shows a spectrum from 1-km altitude obtained on 6 October 1999. For the data shown, the background was subtracted and normalized. Still, a significant amount of signal underlies the aerosol peak, and much of this signal is due to molecular backscatter. We determined the portion that is due to the contrast by calculating the ratio of the maximum signal to the minimum signal in the reference spectrum for a given peak. The return in subsequent altitude bins was then separated into the aerosol and molecular components by (refer to Fig. 7)

$$M(j) = \frac{CT_{\min} - T_{\max}}{C - 1}, \tag{2}$$

where $M(j)$ is the molecular signal in spectral bin j and C is the contrast (ratio of the maximum signal $T_{\max}$ to the minimum signal $T_{\min}$ in the reference bin). This derivation assumes that the molecular signal is flat over the width of the aerosol peak, which is a good assumption given the difference in widths of the two spectral shapes. With the signal separated into the two components, we find the scattering contribution of each to the signal by taking the integral under each curve over one full order of the aerosol channel. The A/M backscatter ratio is then generally expressed in terms of the total-to-molecular ratio $(1 + A/M)$.

4. Measurements

A. Aerosol Measurements

Because only one component of the wind vector was to be obtained during this initial study, the telescope and laser assembly was aligned facing west for each of the days that data collection was performed. West was chosen as the direction of alignment because winds are generally from this direction in the lower atmosphere at the latitude of the instrument

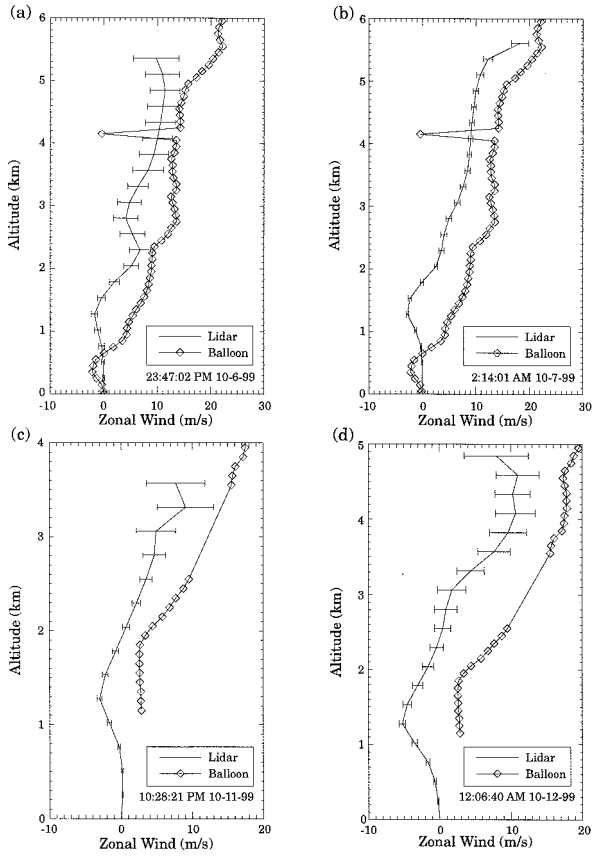

Fig. 8. Plots showing 10-s lidar wind profiles compared with a rawinsonde launched ~10 km away. Error bars at each altitude represent $\pm 1\sigma$ for all data files in a data set. All times are EDT.

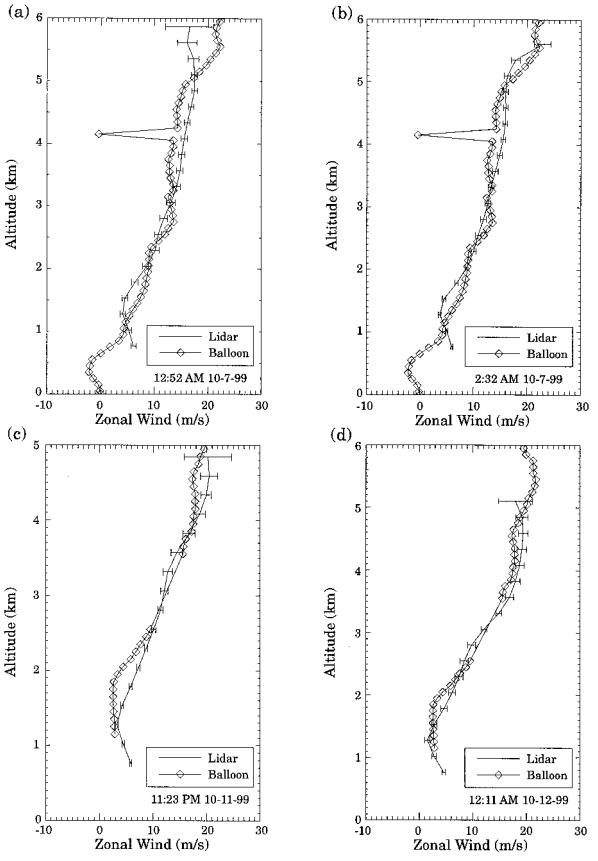

Fig. 9. Plots showing 3.5-min lidar profiles compared with the balloon. All times are EDT. A 6.24-m/s offset was applied to the lidar soundings.

(42 °N). Examination of the rawinsonde data verified that the winds were primarily from the west.

Example measurements of winds taken with the U of M Doppler lidar instrument are shown in Figs. 8 and 9. Figure 8 shows zonal winds calculated from 10 s of lidar data for two different nights in October 1999, and Fig. 9 shows data integrated over a period of 3.5 min (one complete data file) for the same nights. The data files selected for display were randomly picked (one from each data set) for each day. Although errors in wind measurements are readily quantified when a full inverse model has been developed and properly calibrated, it is more difficult to quantify these parameters when the DFT is used to perform the inversion. The error bars in Figs. 8 and 9 provide an estimate, however, and represent the standard deviation of each altitude point over the course of a data set (roughly a two-hour period).

A profile of the zonal winds measured by a rawinsonde launched ~10 km away from the lidar is also shown in Figs. 8 and 9. It is important to note several details from each of these plots. Lidar data are plotted for points where the standard deviation from the mean velocity was less than 5 m/s. For the 6–7 October data [Figs. 9(a) and 9(b)] this included all points below 5.87-km altitude; for 11–12 October [Figs. 9(c) and 9(d)] it includes all points below 4.85 km. As discussed below, these measurements correspond to altitudes where more than ~2% of the backscattered light is due to aerosol scattering. The balloon data are generally taken to be the standard (i.e., it is assumed that there are no errors in the balloon data), and the lidar measurements are typically assumed to be in error when a comparison such as this is performed. Although the lidar measurements are indeed in error (which is also discussed below), the balloon data from each day do indicate that the balloon measurements are far from perfect. Two large holes in the balloon data are noted from the ground to 1.1-km altitude and from 2.6- to 3.5-km altitude in the 11 October data. The spurious data point in the 7 October balloon sounding is likely due to an error in the balloon's location as determined by the tracking equipment. Still, the error in the balloon measurement is assumed to be ± 0.5 m/s for all data points.

It was expected that an offset would need to be applied to lidar wind measurements because of the different optical paths of the reference and return signals, which led to differences in illumination between the two signals. The best way to determine this offset would be to compare the lidar data with a statistically significant sample of balloon soundings over a period of several days. Time constraints did

not allow this to be done with the present system. However, it was noted that there was a fairly consistent difference between the lidar- and balloon-measured velocities and that this difference was roughly the same for each day. The average difference for all soundings between 1-km altitude and the maximum attainable altitude for each day was 6.24 m/s, and this was added to the lidar soundings of Fig. 9. The lowest three points were omitted from Fig. 9 because the overlap between the reference signal and the return signal on the CCD creates an indeterminate offset in this region.

Although it is not possible to draw a firm conclusion from this data given the low number of balloon soundings, good agreement is nonetheless obtained between the lidar and the balloon for the soundings shown in Fig. 9. Comparing Figs. 8 and 9 with the data taken with the first-generation U of M lidar[8,19,20] shows the significant gains realized with this lidar system: Accurate wind measurements could be made only to ~1.5 km over periods from 2 to 30 min with the first instrument, whereas data from over 5-km altitude were obtained with the new instrument with less than 10 s of actual integration time. Furthermore, comparison of the expected spectral response computed from a forward model[17] with the actual response from the aerosol channel showed agreement to within a factor of ~3. This was within the expected results. Because aerosol concentrations are highly variable, the model can serve only as an order-of-magnitude estimate for the aerosol-backscattering contribution.

An in-depth examination was presented by McGill *et al.*[20] that described what value of the A/M ratio was necessary to effect a wind measurement with the first-generation U of M lidar for a given count rate. It is not possible at this time to repeat that analysis for the present system because of the low number of lidar and balloon profiles. However, Fig. 10 shows the corresponding A/M ratio plots for the soundings of Fig. 9 in an effort to estimate what ratios are necessary to effect a measurement with the current system. The ratio is plotted on a log scale to illustrate that, although the ratio is low between 2 and 3 km for the 6–7 October data and between 3 and 5 km for the 11–12 October data, there is still a small contribution that is due to aerosol scattering. The data point at 2.5 km in Fig. 9(b) has a value of only 1.02 (2% aerosol scattering), yet a precise measurement (σ = 0.46 m/s) of the wind is still obtained at this altitude. However, the ratio at 6.9 km in Fig. 9(b) is much higher (1.09), but the wind measurement at this altitude greatly differs from the balloon (11.7 m/s; recall that the average for all other points up to 5 km was ~6 m/s different from the balloon sounding). The reason for this discrepancy (as was also the case for McGill *et al.*) is due to the decrease in the count rate with increasing altitude. The count rate at 2.5 km was still ~23% of the peak aerosol level, whereas the 6.9-km data dropped to ~0.04% of the peak aerosol counts seen on the detector. It was noted that, on these two days, when the ratio fell below 1.02, no precise wind measurement was obtained. The ratio never dropped below 1.02 below 5 km, however, and the aerosol counts had dropped only to 0.3% of the peak aerosol counts by that altitude.

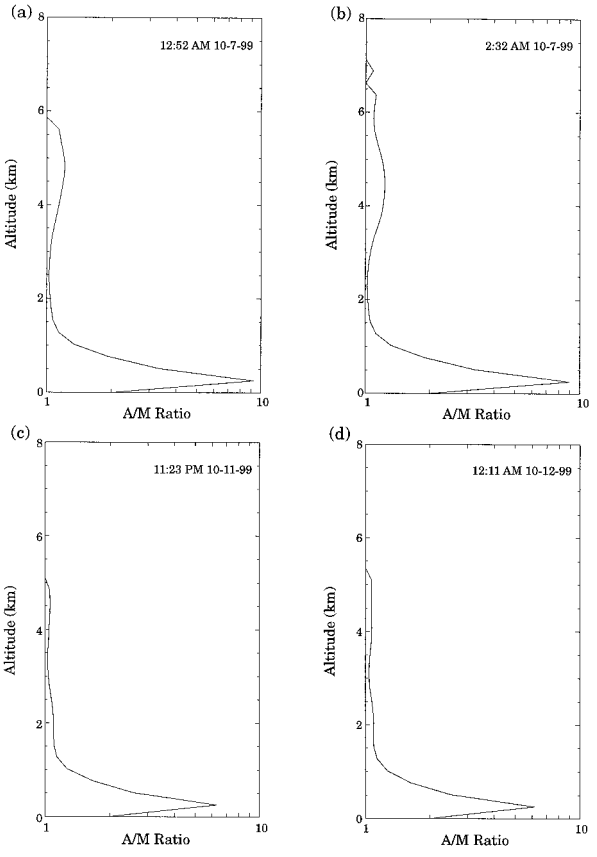

Fig. 10. A/M ratio corresponding to the soundings in Figs. 8 and 9.

B. Molecular Measurements

One of the objectives of this study was to demonstrate that light reflected from the aerosol etalon could be captured, passed through the molecular etalon, and imaged onto a second CCD detector. Although this was indeed the case, wind measurements could not be performed because use of the CLIO cone maps etalon defects onto the resultant image. This problem can be corrected, but requires significant modifications to the present instrument, as described below. In this section we first discuss this limitation, as well as the instrument upgrades necessary to effect molecular wind measurements. Then unprocessed spectra are shown to demonstrate proof of concept when reflected light from the aerosol etalon is used.

In a typical application with Fabry–Perot interferometers, the light rays that form the fringe pattern on the detector come from all parts of the etalon. According to Fabry–Perot interferometry theory, all light rays passing through the etalon with the same angle of incidence are all imaged to the same point, and there is no relation between the points on the

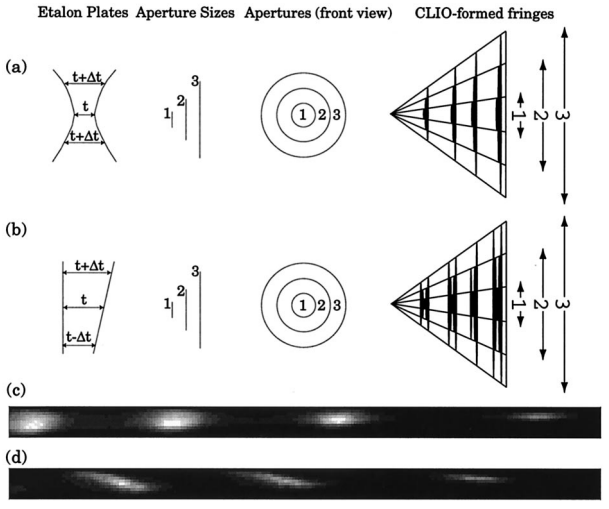

Fig. 11. Effect of etalon plate errors on the CLIO-formed spot. Each numbered aperture maps to the region of the wedge indicated. (a) The etalon plates are bowed, so each increasing aperture size maps a fringe slightly offset from the preceding aperture because t increases radially outward. (b) The etalon plates are tilted along the axis of the cone. In this case, each increasing aperture maps a portion of the fringe farther from the cone apex and a portion of the fringe closer to the cone apex because the aperture maps a portion of the etalon with below-nominal plate spacing and a portion of the etalon above-nominal plate spacing. (c) and (d) A tilt of the etalon perpendicular to the axis of the cone is illustrated experimentally. In (c), the etalon is roughly aligned, so the CLIO-formed spots are round. In (d), the plates were misaligned by compression of an etalon post whose position lies on a line perpendicular to the axis of the cone. The result is the slanted fringes shown.

etalon and the image plane. This is not true when the CLIO is used. Use of the CLIO preserves a relationship between the location on the etalon and the location on the image plane.

The reason for this coherence follows from Hays,[18] where it is shown that the width of the line on the detector formed by the CLIO is inversely proportional to the f/number of the light from the imaging lens. Putting a small enough aperture in front of the imaging lens can thus reduce the width of the image, illustrating that the center of the etalon is imaged to the center of the CLIO-formed wedge. As the aperture size is increased, the wedge grows in width, and outer portions of the etalon are mapped to wider and wider triangular regions of the wedge. This is illustrated in Fig. 11 where the effects of different etalon defects are shown. The etalon defects shown in Fig. 11 are greatly exaggerated for clarity; however, small-scale effects can have a significant impact on the measurement. The result is an apparent Doppler shift across the unshifted reference line, which introduces error into the wind measurement. This effect is not as profound in the aerosol channel, where the fringes are only 88.75 m/s apart (i.e., a 1% shift across the line translates to 0.89-m/s error), but is quite sizable in the molecular channel where the fringes are 3328 m/s apart. Because a $\lambda/2$ (177.5-nm) change in plate spacing changes the order of interference by one, to achieve 2-m/s wind accuracy with the molecular channel, the plates must be parallel to $\sim\lambda/3000$. An estimate of the degree of tilt between the plates can be obtained from the typical flatness value of the plates, $\sim\lambda/200$. A fine-thread screw compressing a spring-loaded bushing adjusts the length of each etalon post, and $\lambda/200$ is about the best that can be achieved by hand. This means that the best possible wind error that could be achieved without hardware modifications is $\sim$30 m/s. With the aerosol channel, however, the flatness specification for a 1-m/s error is less than $\lambda/200$, which explains why aerosol wind measurements were more easily obtained.

If the illumination received from the sky were uniform, this effect could easily be compensated for in the analysis software. Unfortunately, the return from the sky is not uniform. The only way to adequately remove the effect is to precisely tune the etalon plate spacing to interactively correct for any small tilts that may exist. This can be done by use of servo-controlled piezoelectric etalon posts such as were used on the High Resolution Doppler Imager aboard the Upper Atmosphere Research Satellite.[27] When the post spacing is adjusted to maximize the etalon finesse, the tilt can be effectively reduced to zero, and wind measurements can be made with less than 2-m/s error.[28]

However, this effect could not be adequately compensated in the current lidar instrument for the early testing phase, so the results shown here do not include wind velocities from molecular backscatter. Still, a comparison of return light received by the molecular channel with the forward model is made to illustrate that the capability does indeed exist. Figure 12(a) shows the return signal from a 5-km range as well as the forward model prediction of the expected return. Comparing this with Fig. 7, it can be seen that there is no significant background underlying the return signal, indicating that this signal is mostly molecular backscatter (the background was removed and the data were normalized). The model data in Fig. 12 were scaled to match the response to the return data.

The potential to measure molecular winds to extended ranges is illustrated by the spectra of Fig. 12(b). These data are from the 9.7- and 11.2-km range (6.9- and 7.9-km altitude). Because the data are noisy, the 9.7-km data are shown to demonstrate that the 11.2-km data show signal and are not just noise. The noise was due to a malfunction with the molecular channel CCD detector, which resulted in an increase in the read noise by approximately a factor of 4. This limited the maximum obtainable range because the measurements dropped to the noise floor much more quickly than with a properly operating CCD. The data of Fig. 12(b) are also shown only for a portion of the line because the effect of the noise was more severe toward the center of the fringe pattern. A new CCD chip with typical noise characteristics would easily overcome this problem

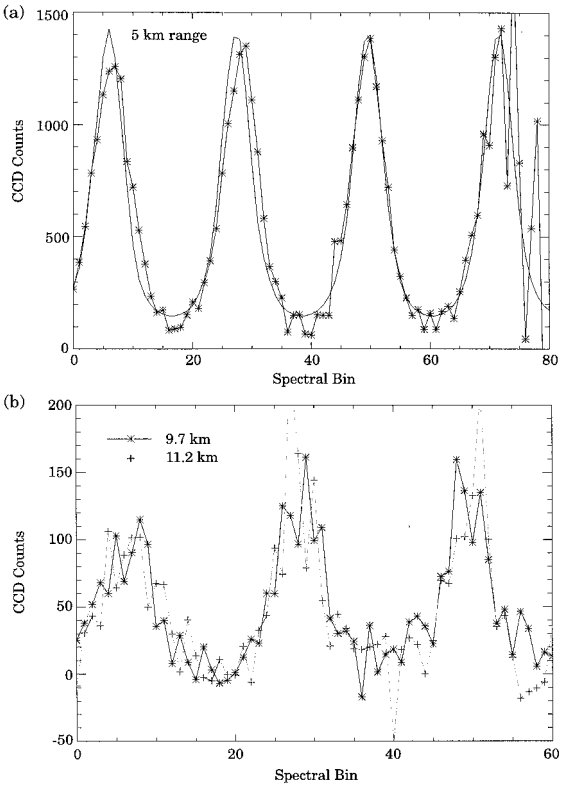

Fig. 12. (a) Comparison of the forward model with lidar data from a 5-km range on 15 November 1999. The model data were divided by a factor of 22.1 to match the model and data response. (b) Molecular channel spectra from a 9.7- and 11.2-km range (6.9- and 7.9-km altitude).

and, together with proper alignment, should extend measurements into the stratosphere.

5. Conclusion

An instrument has been described that demonstrates a combination of techniques to optimize the return signal from a direct-detection Doppler lidar. The main improvement involves use of a CCD detector that, to our knowledge, has not been previously employed in a working lidar system. Quantum efficiencies several times higher than those obtained with photomultiplier-type devices are achieved with this type of detector. Implementation of this technology was made possible through use of a reflective cone (CLIO) to convert the circular fringes from a Fabry–Perot etalon into a linear series of spots on the CCD. Once converted to a linear pattern, altitude resolution is obtained when the data on the CCD are shifted along an axis perpendicular to the arrangement of spots on the detector. Reverse shifting of the charge by use of a specially designed controller allows integration of return signal on the chip, which improves the signal-to-noise ratio and extends the range of measurement.

Another technology that was demonstrated is use of the reflected signal from the primary (aerosol) etalon and subsequent use of this signal in a wider-bandwidth (molecular) etalon. Although previous lidar systems have not made use of this reflected light, the U of M lidar system employs the reflected signal by the implementation of a second CCD detector and CLIO imaging system. This allows not only a significant increase in system throughput, but also allows measurements to be made with both molecular and aerosol backscatter simultaneously. In addition, a third CCD can be used to capture this reflected light, and in this manner practically all the signal entering the receiving optics can be used effectively.

One limitation of the CLIO device is that defects in etalon plate spacing are mapped onto the detector. For small-bandpass devices, such as the aerosol etalon, this does not present a major problem. For the larger-bandpass molecular etalon, however, this limitation has prevented wind measurements from molecular backscatter from being made at this time. Another difficulty presented by the CLIO is that data from successive altitudes overlap one another to an increasing degree as distance from the cone apex increases. This requires a more sophisticated analysis algorithm to be employed to derive the wind velocities from the raw spectral data. Both of these difficulties have been overcome with a new improved version of the lidar system by one of the authors, which will be the subject of a future publication.

The authors thank the reviewers for their particularly helpful comments. This research was largely supported by internal research funds at the University of Michigan.

References

1. P. K. Rao, S. J. Holmes, R. K. Anderson, J. S. Winston, and P. E. Lehr, eds., *Weather Satellites: Systems, Data, and Environmental Applications* (American Meteorological Society, Boston, Mass., 1990).
2. D. Atlas and C. L. Korb, "Weather and climate needs for lidar observations from space and concepts for their realizations," Bull. Am. Meteorol. Soc. **62,** 1270–1285 (1981).
3. A. V. Jelalian and R. M. Huffaker, "Application of laser Doppler techniques to turbulent velocity measurement. Part II: Laser Doppler techniques for remote wind velocity measurements," in *Specialist Conference on Molecular Radiation and its Application to Diagnostic Techniques*, NASA Tech. Memo. TMX-53711, R. Goulord, ed., (NASA Marshall Space Flight Center, Huntsville, Ala. 1967), pp. 345–356.
4. R. M. Huffaker, D. W. Beran, and C. G. Little, "Pulsed coherent lidar systems for airborne and satellite based wind field measurement," in *Seventh Conference on Aerospace and Aeronautical Meteorology and Symposium on Remote Sensing from Satellite* (American Meteorological Society, Boston, Mass., 1976), pp. 318–324.
5. V. J. Abreu, "Wind measurements from an orbital platform using a lidar system with incoherent detection: an analysis," Appl. Opt. **18,** 2992–2297 (1979).
6. D. Rees and I. S. McDermid, "Doppler lidar atmospheric wind sensor: reevaluation of a 355-nm incoherent Doppler lidar," Appl. Opt. **29,** 4133–4144 (1990).
7. R. J. Curran, "NASA's plans to observe the Earth's atmosphere with lidar," IEEE Trans. Geosci. Remote Sens. **27,** 154–163 (1989).
8. M. J. McGill, W. R. Skinner, and T. D. Irgang, "Analysis techniques for the recovery of winds and backscatter coefficients

from a multiple-channel incoherent Doppler lidar," Appl. Opt. **36,** 1253–1268 (1997).
9. M. L. Chanin, A. Garnier, A. Hauchecorne, and J. Porteneuve, "A Doppler lidar for measuring winds in the middle atmosphere," Geophys. Res. Lett. **16,** 1273–1276 (1989).
10. V. J. Abreu, J. E. Barnes, and P. B. Hays, "Observations of winds with an incoherent lidar detector," Appl. Opt. **31,** 4509–4514 (1992).
11. J. W. Bilbro, "Atmospheric laser Doppler velocimetry: an overview," Opt. Eng. **19,** 533–542 (1980).
12. F. M. Ralph, P. J. Neiman, T. L. Keller, D. Levinson, and L. Fedor, "Observations, simulations, and analysis of nonstationary trapped lee waves," J. Atmos. Sci. **54,** 1308–1333 (1997).
13. R. M. Huffaker and R. M. Hardesty, "Remote sensing of atmospheric wind velocities using solid-state and CO_2 coherent laser systems," Proc. IEEE **84,** 181–204 (1996).
14. R. T. Menzies, "Doppler lidar atmospheric wind sensor: a comparative performance evaluation for global measurement applications from Earth orbit," Appl. Opt. **25,** 2546–2553 (1986).
15. C. A. Tepley, S. I. Sargoytchev, and R. Rojas, "The Doppler Rayleigh lidar system at Arecibo," IEEE Trans. Geosci. Remote Sens. **31,** 36–47 (1993).
16. C. L. Korb, B. M. Gentry, and C. Y. Weng, "Edge technique, theory and application to the lidar measurement of atmospheric wind," Appl. Opt. **31,** 4202–4213 (1992).
17. W. R. Skinner and P. B. Hays, "Incoherent Doppler lidar for measurement of atmospheric winds," in *Optical Spectroscopic Techniques and Instrumentation for Atmospheric and Space Research*, J. Wang and P. B. Hays, eds., Proc. SPIE **2266,** 383–394 (1994).
18. P. B. Hays, "Circle to line interferometer optical system," Appl. Opt. **29,** 1482–1489 (1990).
19. K. W. Fischer, V. J. Abreu, W. R. Skinner, J. E. Barnes, M. J. McGill, and T. D. Irgang, "Visible wavelength Doppler lidar for measurement of wind and aerosol profiles during day and night," Opt. Eng. **34,** 499–511 (1995).
20. M. J. McGill, W. R. Skinner, and T. D. Irgang, "Validation of wind profiles measured with incoherent Doppler lidar," Appl. Opt. **36,** 1928–1939 (1997).
21. T. D. Irgang, "Direct-detection Doppler lidar employing a CCD detector: design and early measurements," Ph.D. dissertation (University of Michigan, Ann Arbor, Mich., 2000).
22. L. A. Rahn, "Feedback stabilization of an injection-seeded Nd:YAG laser," Appl. Opt. **24,** 940–942 (1985).
23. J. A. McKay, "Single and tandem Fabry–Perot etalons as solar background filters for lidar," Appl. Opt. **38,** 5851–5858 (1999).
24. W. V. Houston, "A compound interferometer for fine structure work," Phys. Rev. **29,** 478–484 (1927).
25. J. M. Vaughan, *The Fabry–Perot Interferometer: History, Theory, Practice and Applications* (Hilger, Philadelphia, Pa., 1989).
26. I. M. Povey, A. M. South, A. t'Kint de Roodenbeke, C. Hill, R. A. Freshwater, and R. L. Jones, "A broadband lidar for the measurement of tropospheric constituent profiles from the ground," J. Geophys. Res. **103,** 3369–3380 (1998).
27. P. B. Hays, V. J. Abreu, M. E. Dobbs, D. A. Gell, H. J. Grassl, and W. R. Skinner, "The high resolution Doppler imager on the upper atmosphere research satellite," J. Geophys. Res. **98,** 10713–10723 (1993).
28. P. B. Hays and C. A. Nardell, "The GroundWinds New Hampshire instrument and the LIDAR-Fest 2000 campaign," presented at the SPIE Forty-Sixth International Symposium on Optical Science and Technology, San Diego, Calif., 29 July–3 Aug. 2001.